Chinese Chemical Letters 32 (2021) 2524–2528

Contents lists available at ScienceDirect

Chinese Chemical Letters

journal homepage: www.elsevier.com/locate/cclet

Communication

Tuning the concentration of surface/bulk oxygen vacancies in CeO_2 nanorods to promote highly efficient photodegradation of organic dyes

Zhen Shen[a,b,1], Yipeng Zhou[a,1], Yue Guo[b], Jie Zhao[a,b,**], Jianhua Song[a], Yu Xie[a,*], Yun Ling[a], Wei Zhang[c,*]

[a] Department of Material Chemistry, Nanchang Hangkong University, Nanchang 330063, China
[b] School of Chemistry and Chemical Engineering, Nanjing University, Nanjing 210023, China
[c] School of Ecology and Environment Science, Zhengzhou University, Zhengzhou 450001, China

ARTICLE INFO

Article history:
Received 20 November 2020
Received in revised form 23 December 2020
Accepted 22 January 2021
Available online 27 January 2021

Keywords:
CeO_2
Nanorods
Oxygen vacancy
Photodegradation
Organic pollutant

ABSTRACT

To enhance the photodegradation ability of CeO_2 for organic dyes, an effective strategy is to introduce oxygen vacancies (V_o). In general, the introduced V_o are simultaneously present both on the surface and in the bulk of CeO_2. The surface oxygen vacancies ($V_{o\text{-}s}$) can decrease the band gap, thus enhancing light absorption to produce more photogenerated e^- for photodegradation. However, the bulk oxygen vacancies ($V_{o\text{-}b}$) will inhibit photocatalytic activity by increasing the recombination of photogenerated e^- and $V_{o\text{-}b}$. Therefore, regulating the concentrations of $V_{o\text{-}s}$ to $V_{o\text{-}b}$ is a breakthrough for achieving the best utilization of photogenerated e^- during photodegradation. We used an easy hydrothermal method to achieve tunable concentrations of $V_{o\text{-}s}$ to $V_{o\text{-}b}$ in CeO_2 nanorods. The optimized CeO_2 presents a 70.2% removal of rhodamine B after 120 min of ultraviolet–visible light irradiation, and a superior photodegradation performance of multiple organics. This tuning strategy for V_o also provides guidance for developing other advanced metal-oxide semiconductor photocatalysts for the photodegradation of organic dyes.

As a green and sustainable technology, photocatalysis has been increasingly studied due to its great potential in solving environmental pollution and energy crises [1–3]. In photocatalytic processes, photoactive materials, such as TiO_2 [4], CeO_2 [5], $ZnCo_2O_4/Bi_2O_3$ [6], g-C_3N_4/Ag_3PO_4 [7], SnO_2 [8], BiOBr/TiO_2/$Ti_3C_2T_X$ [9], GaN [10], CdS [11], and $BiVO_4/Znln_2S_4$ [12] play decisive roles in the redox/charge-transfer reactions due to their unique electronic structures with a filled valence band (VB) and an empty conduction band (CB) [1]. Among them, CeO_2 has been widely used in industry because Ce, as a rare-earth element, has a low price and relatively high abundance in the Earth's crust. As an n-type semiconductor (with a band gap similar to that of TiO_2), it exhibits potential photocatalytic activity. However, the wide band gap restricts its photocatalytic efficiency [4,13]. Considering this, other components, including semiconductors and metals, have been introduced to improve UV and/or visible light absorption and prevent hole-electron recombination [14–17]. Moreover, the modification of CeO_2 by controlling its size, morphology, and number of defects will be significant for improving its intrinsic photocatalytic properties [18,19].

Nanoscale CeO_2, *e.g.*, nanoparticles, nanosheets, and nanorods, can effectively enhance UV and/or visible light absorption and promote the adsorption of reactants due to its high specific surface area, thereby facilitating photocatalytic reactions [20]. Previous studies have mainly focused on the comparison of photocatalytic performance with different morphologies of CeO_2 [21,22]. However, the intrinsic photocatalytic performance of CeO_2 still needs to be further studied, especially the effect of defects on its catalytic performance, which needs to be studied with the same morphology or even uniform size. One-dimensional (1D) CeO_2 nanorods with well-defined {100} and {110} planes show better photocatalytic performances than other stable polyhedral-structured CeO_2 [13]. Additionally, the 1D nanorod structure dramatically improves the redox properties because of its more efficient and fast transport of photogenerated e^- and h^+ along the nanorod surface [23–26].

Defects in catalysts are crucial factors affecting photocatalytic performance. The defect formation energies in nanomaterials are lower due to the existence of a high-density interface, which leads

* Corresponding authors.
** Corresponding author at: Department of Material Chemistry, Nanchang Hangkong University, Nanchang 330063, China.
E-mail addresses: zhaojienju@163.com (J. Zhao), xieyu_121@163.com (Y. Xie), zhangwei88@zzu.edu.cn (W. Zhang).
[1] These authors contributed equally to this work.

https://doi.org/10.1016/j.cclet.2021.01.044
1001-8417/

to an increase in nonstoichiometric defects and the generation of electron carriers [27]. In addition, Ce ions usually show two valences (Ce^{3+} and Ce^{4+}) due to their special outer electron structure of [Xe] $4f^2 6s^2$, thus tending to form multivalent oxides of CeO_{2-x} ($x = 0 - 0.5$) [13]. Therefore, a large number of oxygen vacancies (V_o) are easily formed on/in the surface/bulk of CeO_2. Many strategies have been developed for the introduction of oxygen vacancies to CeO_2 by using reductant including H_2, CO, NH_3, and Li [28–30]. These V_o are present both on the surface and in the bulk phase. The surface oxygen vacancies ($V_{o\text{-}s}$) can promote the increase in the Fermi level attributed to the generation of defect energy levels (near the bottom of the CB in CeO_2) in the band gap, leading to a narrowed band gap and enhanced light absorption [31]. In addition, coordinative-unsaturated metal atoms (surrounding V_o) can act as strong binding sites for organic dyes, thus accelerating photocatalytic reactions [32,33]. Moreover, bulk oxygen vacancies ($V_{o\text{-}b}$) may act as recombination centers of photogenerated e^- coming from the surface, resulting in a low utilization of photogenerated e^- [34]. With an increasing concentration ratio (from $V_{o\text{-}s}$ to $V_{o\text{-}b}$), the utilization of photogenerated e^- for photodegradation can be improved, thus leading to improved photocatalytic performance [35–37]. Therefore, the precise regulation of V_o is of great significance to improve the intrinsic photocatalytic performance of CeO_2 when applied to the degradation of organic dyes.

Herein, we synthesize and report a 1D CeO_2 nanorod with uniform size and morphology. The hydrothermal method is used to tune the concentration ratio of surface/bulk oxygen vacancies in CeO_2 nanorods. With the highest concentration of $V_{o\text{-}s}$ to $V_{o\text{-}b}$, the CeO_2 nanorod presents the narrowest band gap and the highest utilization of photogenerated e^-. In regard to the photodegradation of rhodamine B, the percentage of removal reaches 70.2% after 120 min of ultraviolet–visible light irradiation, exhibiting potential application in wastewater purification. This tuning strategy of V_o also provides guidance for the development of other advanced metal-oxide semiconductor photocatalysts for the photodegradation of organic dyes.

The X-ray powder diffraction (XRD) patterns of the as-prepared CeO_2-1, CeO_2-2, and CeO_2-3 are shown in Fig. 1a. The diffraction peaks of the catalysts were mainly assigned to the (111), (200), (220), (311), (222), (400), and (331) planes, which were indexed to the cubic fluorite structure of CeO_2 crystals (JCPDS No. 34-0394). The field-emission scanning electron microscopy (FESEM) and transmission electron microscopy (TEM) images of CeO_2-1, CeO_2-2, and CeO_2-3 are shown in Figs. 1b and c and Fig. S1 (Supporting information), respectively. All the samples are 1D nanorod structures. The shorter and narrower CeO_2-1 and CeO_2-2 nanorods loaded with small nanoparticles led to irregular surfaces with rough structures (Fig. 1c and Fig. S1). CeO_2-3 exhibited longer and broader nanorods with smooth surfaces (Fig. S1d). Furthermore, two types of interference fringes of 0.19 and 0.31 nm were observed at the outer and inner nanorods from the high resolution transmission electron microscopy (HRTEM) image, which could be assigned to the (220) and (111) planes of the cubic fluorite structure CeO_2, respectively (Fig. 1d). This result suggests that the preferred orientation growth of the individual CeO_2-2 nanorods was along the [110] direction and that the main exposed crystal surface was the (220) plane, which had a higher photocatalytic activity than (111). In addition, an ~5 nm CeO_2 nanoparticle on the CeO_2-2 surface could be clearly seen, which likely formed during the initial crystal growth processes after the distribution of nucleation sites. Moreover, CeO_2-2 exhibited a Brunauer-Emmett-Teller (BET) surface area of 137 m^2/g, which was larger than those of CeO_2-1 and CeO_2-3 (52 and 47 m^2/g, respectively) (Fig. S2 in Supporting information). Clearly, this large BET specific surface area was mainly attributed to its rough surface (Fig. 1c), thus providing abundant active sites and more $V_{o\text{-}s}$. These $V_{o\text{-}s}$ were conducive to enhanced light absorption and reactant adsorption; additionally, the exposed (220) facets contributed to the high reactive activity, and both factors improved the photocatalytic performance of CeO_2-2 nanorods.

At present, several detection technologies can be used to resolve the V_o in metal oxides, such as, Raman spectrum, extended X-ray absorption fine structure spectroscopy (EXAFS), positron annihilation lifetime spectroscopy (PALS), electron paramagnetic resonance spectrum (EPR), aberration-corrected transmission electron microscopy (ACTEM), electron energy loss spectroscopy (EELS), and X-ray photoelectron spectroscopy (XPS) [38,39]. Among those detection method, Raman, EXAFS, PALS, and EPR are often used to analyze the total V_o information in catalyst, while the ACTEM, EELS, and XPS are often used to analyze V_o in the local or surface of catalyst. In this paper, we combined Raman and XPS to semi-quantitatively analyze the concentration ratio of surface/bulk V_o in CeO_2.

The Raman spectra providing the V_o information of the total crystal, including the bulk and surface, are shown in Fig. 2a. The

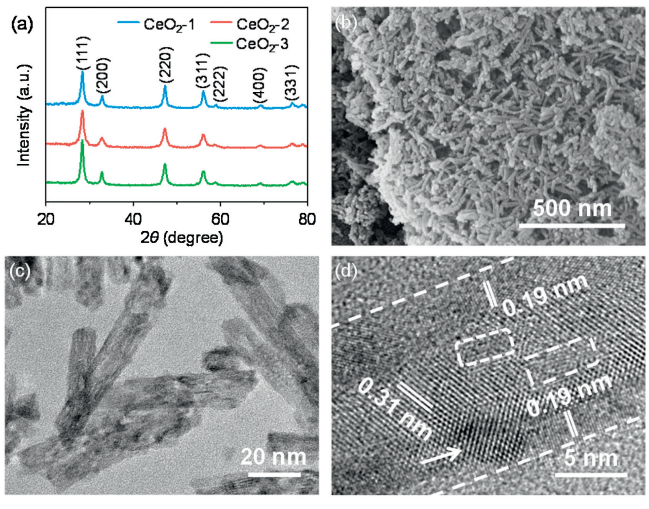

Fig. 1. Structure and morphology. (a) XRD patterns. (b-d) FESEM, TEM, and HRTEM images of CeO_2-2. The pore defects and nanoparticles are marked by white dashed rectangles and arrows, respectively.

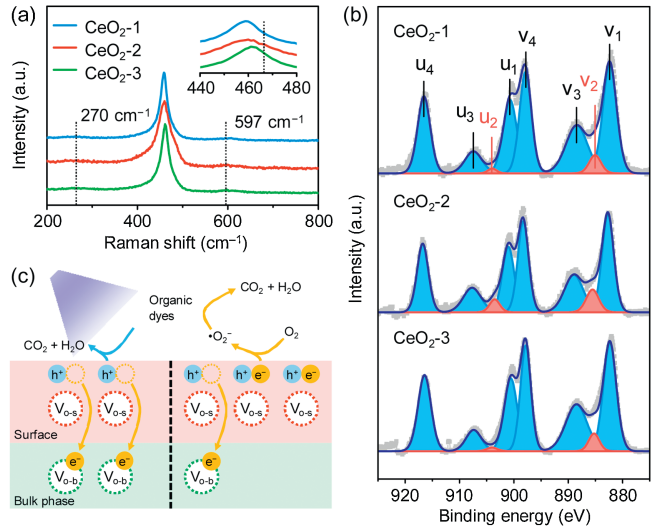

Fig. 2. Tuning surface/bulk oxygen vacancies. (a) Raman spectra. (b) XPS Ce 3d spectra. (c) Schematic action mechanism at different surface/bulk oxygen vacancy ratios.

sharp Raman peaks of CeO_2-1, CeO_2-2, and CeO_2-3 were located at frequencies of 459, 459, and 461 cm^{-1}, respectively, and these were attributed to the first-order vibrational mode with F_{2g} vibration (symmetrical stretching mode of the Ce–O_8 vibration unit) in a fluorite cubic structure. Compared with the reported value of 466 cm^{-1}, the redshifts of the F_{2g} vibration peaks were ascribed to the nanocrystalline nature of CeO_2 [40]. The peak shifts of CeO_2-1 and CeO_2-2 were larger than those of CeO_2-3, further indicating the smaller crystal grains of CeO_2-1 and CeO_2-2. The broader peaks at approximately 270 and 597 cm^{-1} corresponded to the second-order transverse acoustic mode and the defect (D) vibration (*i.e.*, V_o), respectively [17,41]. The $I(D)/I(F_{2g})$ ratios of CeO_2-1, CeO_2-2, and CeO_2-3 were estimated to be 0.048, 0.047 and 0.043, respectively, indicating all three had similar total V_o concentrations (Fig. S3 and Table S1 in Supporting information).

The Ce 3d XPS spectra presented the chemical state of elemental Ce (Fig. 2b). All the peaks could be mainly attributed to the spin – orbital doublet peaks of Ce $3d_{5/2}$ and $3d_{3/2}$, which could be deconvolved into four pairs, *i.e.*, v1 (882.7 eV)/u1 (901.0 eV), v2 (885.4 eV)/u2 (903.7 eV), v3 (889.2 eV)/u3 (907.5 eV), and v4 (898.4 eV)/u4 (916.7 eV) [42,43]. Among them, the v1/u1, v3/u3, and v4/u4 peaks referred to the Ce^{4+} 3d states, while the v2/u2 peak corresponded to the Ce^{3+} 3d states, indicating the composition of Ce^{4+} and Ce^{3+} in these CeO_2. This absence of Ce^{3+} provided evidence of lattice oxygen depletion, further illustrating the existence of V_o on CeO_2 surfaces. The surface oxygen vacancies, *i.e.*, $V_{o\text{-}s}$, could decrease the band gap, thus enhancing light absorption and promoting photogenerated e^- for photocatalysis. The Ce^{3+}/Ce^{4+} ratios of CeO_2-1, CeO_2-2, and CeO_2-3 were estimated to be 4.1%, 8.0%, and 3.8%, respectively, indicating that the order of $V_{o\text{-}s}$ concentration was CeO_2-2 > CeO_2-1 > CeO_2-3. Combining the Raman analysis (the total V_o concentrations in the order of CeO_2-2 ≈ CeO_2-1 ≈ CeO_2-3) with the XPS results (the $V_{o\text{-}s}$ concentrations in the order of CeO_2-2 > CeO_2-1 > CeO_2-3), the order of $V_{o\text{-}b}$ concentrations should be CeO_2-2 < CeO_2-1 < CeO_2-3. Therefore, the concentration ratio of $V_{o\text{-}s}$ to $V_{o\text{-}b}$ was in the order of CeO_2-2 > CeO_2-1 > CeO_2-3 (Table S1 in Supporting information). Fig. 2c illustrates the action mechanism of photodegradation by V_o under different concentration ratios of $V_{o\text{-}s}$ to $V_{o\text{-}b}$. Briefly, h^+/e^- pairs would be generated under irradiation and migrate to the surface of CeO_2, followed by their participation in catalytic reactions. During the migration process, a fair number of photogenerated e^- may be captured by $V_{o\text{-}b}$ and become invalid [35]. A higher concentration ratio of $V_{o\text{-}s}$ to $V_{o\text{-}b}$ led to more photogenerated h^+/e^- pairs and less recombination, which would improve the utilization of photogenerated e^-. In contrast, in the case of a low ratio of $V_{o\text{-}s}$ to $V_{o\text{-}b}$, most photogenerated e^- would be depleted by recombination with more $V_{o\text{-}b}$, which would deteriorate the photodegradation activity.

Fig. 3a shows the photocatalytic performances of the as-synthesized CeO_2 nanorods for rhodamine B photodegradation under UV–vis light irradiation. The results showed that 29.8% and 67.4% of rhodamine B was discolored by CeO_2-1 and CeO_2-2, respectively. CeO_2-2 displayed more efficient photocatalytic performance, which was approximately 2.3 times higher than that of CeO_2-1 after 120 min of light irradiation. CeO_2-3 demonstrated little activity for rhodamine B photodegradation, as shown in Fig. 3a. To quantitatively clarify the photocatalytic activities of different catalysts, rhodamine B photodegradation was studied based on the plots of $-\ln(C_t/C_0)$ *versus* time (Fig. 3b) corresponding to the first-order kinetics model with a linear regression mechanism. As shown, the reaction rate constant k value of CeO_2-2 was 0.0093 min^{-1}, which was approximately 2.5 times that of CeO_2-1 (0.0038 min^{-1}). Accordingly, rhodamine B could be easily adsorbed on the CeO_2-2 surface with abundant $V_{o\text{-}s}$ by a first-order kinetics model. In contrast, the rhodamine B hardly

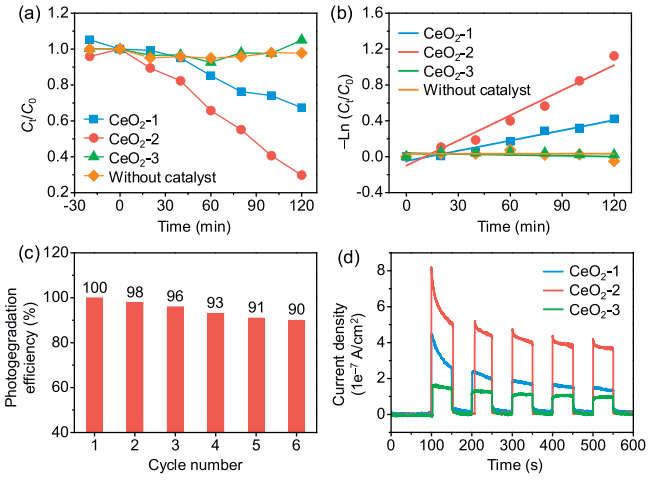

Fig. 3. Photocatalytic degradation performance. (a) Photocatalytic activity of the photodegradation of rhodamine B for 120 min. (b) Corresponding plot of (C_0-C_t) *versus* time. (c) Recycling performance of CeO_2-2. (d) Photocurrent responses.

degraded without photocatalyst under UV–vis light. These experimental results further confirmed that $V_{o\text{-}s}$ played a crucial role in improving photocatalytic activity. Next, we explored the reusability of the catalyst (Fig. 3c). The photocatalytic cycling performance of CeO_2-2 over six cycles slightly decreased for each 120 min run of rhodamine B degradation. These results suggest that CeO_2-2 (with abundant $V_{o\text{-}s}$) was stable and could be reused for rhodamine B photodegradation. For congo red and methyl orange, CeO_2-2 sample also has excellent degradation performance, indicating its application prospect in sewage treatment (Fig. S4 in Supporting information).

The photocurrent responses of the catalysts are shown in Fig. 3d, while the order of photocurrent response was CeO_2-2 > CeO_2-1 > CeO_2-3 under alternating irradiation (lights on and off), which was consistent with the order of the concentration ratio of $V_{o\text{-}s}$ to $V_{o\text{-}b}$. The photocurrent densities based on the BET surface area of three CeO_2 nanorods are similar after 400 s, indicating a negligible effect of surface area on the photocatalytic efficiency in the total photocatalytic processes (Fig. S5 in Supporting information). In regard to the CeO_2-2 sample, its high concentration ratio of $V_{o\text{-}s}$ to $V_{o\text{-}b}$ could ensure that plenty of photogenerated e^- were consumed during photodegradation, corresponding to the largest photocurrent intensity. Moreover, the photocurrent intensities of CeO_2-2 exhibited a very slight decrease during the initial cycles and tended to be flat with increasing time, indicating a stable photoelectric characteristic.

The optical properties and band structures of CeO_2-1, CeO_2-2, and CeO_2-3 were analyzed by UV–vis diffuse reflectance spectroscopy (DRS). Fig. 4a shows that the absorption band edges of CeO_2-1, CeO_2-2, and CeO_2-3 were 428, 436, and 425 nm, respectively, which were higher than that reported for CeO_2 (approximately 420 nm). These redshifts in the absorption bands indicated the quantum confinement effect of 1D-nanostructured CeO_2 nanorods. Furthermore, the absorption band edge of CeO_2-2 exceeded that of other CeO_2 nanorods, suggesting an expanded UV light absorption range and enhanced UV-light-response ability due to its abundant $V_{o\text{-}s}$, which was the reason for its higher photocatalytic efficiency. The band gap energy (E_g) of three samples could be calculated based on the Tauc plot (Eq. 1):

$$(\alpha h\nu)^{1/n} = A(h\nu - E_g) \quad (1)$$

where α, $h\nu$, A, and E_g signify the absorption coefficient, photoenergy, proportionality constant, and band gap energy, respectively. The constant n here equaled 1/2 because CeO_2 is a direct-gap

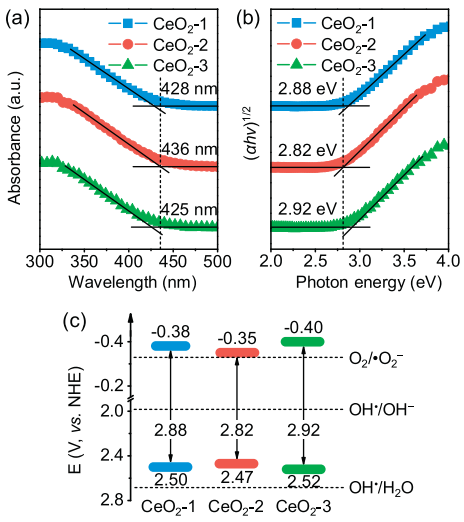

Fig. 4. Band gap analysis. (a) UV–vis diffuse reflectance spectra of the as-prepared samples. (b) Band gap measurement using the Tauc plot. (c) Photodegradation mechanism.

semiconductor. As shown in Fig. 4b, the E_g of CeO_2-1, CeO_2-2, and CeO_2-3 was estimated to be 2.88, 2.82, and 2.92 eV, respectively, exhibiting a lower value compared with that reported for CeO_2 (3.2 eV) [44]. This result could be attributed to the formation of localized states within the band gap due to the V_o and increased Ce^{3+} concentration. Previously, it has been shown that the presence of Ce^{3+} reduces the band gap, leading to an expanded UV light absorption range [45,46]. CeO_2-2 exhibited the narrowest E_g and generated more light-excited carriers under UV irradiation. The evaluated valance band potentials (E_{VB}) of CeO_2-1, CeO_2-2, and CeO_2-3 were +2.50, +2.47, and +2.52 eV, respectively [47]. They were smaller than the required potential for OH radical formation by OH^- ($^{\bullet}OH/H_2O$ pair, +2.68 eV) but larger than that by H_2O ($^{\bullet}OH/OH^-$ pair, +1.99 eV), indicating that the holes in the valance band could directly oxidize rhodamine B but could not oxidize water. The conduction band edge position could be calculated by the following equation (Eq. 2):

$$E_{CB} = E_{VB} - E_g \quad (2)$$

As a result, the conduction band potentials (E_{CB}) of CeO_2-1, CeO_2-2, and CeO_2-3 were calculated to be −0.38, −0.35, and −0.40 eV, respectively, which were larger than the reduction potential for the reduction of molecular oxygen to superoxide anion radicals with strong oxidation ($O_2/^{\bullet}O_2^-$ pair, −0.33 eV), which energetically satisfied the requirements for the degradation of rhodamine B.

Based on the E_g and band edge positions of the CeO_2 nanorods, a photodegradation mechanism was proposed and is shown in Fig. 4c. Excitations (e^-/h^+) were produced when UV–vis light irradiated the CeO_2 nanorods. These charge carriers rapidly transferred to the CeO_2 surface due to the short transfer length in the 1D nanorod structure. The h^+ in the valance band could directly oxidize rhodamine B; simultaneously, the e^- in the conduction band could reduce molecular oxygen to superoxide anion radicals. In regard to the CeO_2-2 sample, the narrow band gap ensured the generation of a large number of photogenerated e^-. The higher concentration ratio of $V_{o\text{-}s}$ to $V_{o\text{-}b}$ improved the utilization of photogenerated e^- because of the fast transfer of photogenerated e^- for photodegradation on the surface and the decreased probability of photogenerated e^- and $V_{o\text{-}b}$ recombination in bulk. Additionally, the high specific surface area of CeO_2-2 provided a large number of adsorption sites for the photodegradation of rhodamine B. Based on the above reasons, the CeO_2-2 sample exhibited the best photodegradation performance.

In summary, we successfully prepared 1D CeO_2 nanorods with a uniform size and morphology. By an easy hydrothermal method, we tuned the concentration of surface/bulk oxygen vacancies in CeO_2 nanorods. With the highest concentration ratio (from $V_{o\text{-}s}$ to $V_{o\text{-}b}$), the CeO_2 nanorod presented more efficient utilization of photogenerated e^- due to the fast transfer of photogenerated e^- for photodegradation on the surface and the decreased probability of photogenerated e^- and $V_{o\text{-}b}$ recombination in bulk. In regard to the photodegradation of rhodamine B, the removal percentage reached 70.2% after 120 min of UV–vis light irradiation, exhibiting potential applications for wastewater purification. This V_o tuning strategy provides guidance for the development of other advanced metal-oxide semiconductor photocatalysts for the photodegradation of organic dyes.

Declaration of competing interest

The authors report no declarations of interest.

Acknowledgments

This work was financially supported by the National Natural Science Foundation of China (Nos. 21404054, 21667019, 22066017, 52000163), the Key Project of the Natural Science Foundation of Jiangxi Province (No. 20171ACB20016), the Jiangxi Province Major Academic and Technical Leaders Cultivating Object Program (No. 20172BCB22014), the Science and Technology Department of Jiangxi Province (Nos. 20181BCB18003, 20181BAB216012, 20181ACG70025, and 20192BAB206013), the Key Laboratory of Photochemical Conversion and Optoelectronic Materials, TIPC, CSA (No. PCOM201906), and the Key Project of Science and Technology Research of the Jiangxi Provincial Department of Education (Nos. DA201602063, GJJ13508, and GJJ191044), the Aviation Science Foundation of China (No. 2017ZF56020), the Fujian Key Laboratory of Measurement and Control System for Shore Environment (No. S1-KF1703), and the Program B for Outstanding PhD Candidate of Nanjing University (No. 202002B076).

Appendix A. Supplementary data

Supplementary material related to this article can be found, in the online version, at doi:https://doi.org/10.1016/j.cclet.2021.01.044.

References

[1] A. Kubacka, M. Fernandez-Garcia, G. Colon, Chem. Rev. 112 (2012) 1555–1614.
[2] T. Hisatomi, J. Kubota, K. Domen, Chem. Soc. Rev. 43 (2014) 7520–7535.
[3] Y. Ma, X. Wang, Y. Jia, et al., Chem. Rev. 114 (2014) 9987–10043.
[4] Q. Guo, C. Zhou, Z. Ma, X. Yang, Adv. Mater. 31 (2019) 1901997.
[5] M. Aslam, M.T. Qamar, M.T. Soomro, et al., Appl. Catal. B: Environ. 180 (2016) 391–402.
[6] J. Chen, J. Zhan, Y. Zhang, Y. Tang, Chin. Chem. Lett. 30 (2019) 735–738.
[7] M. Ding, J. Zhou, H. Yang, et al., Chin. Chem. Lett. 31 (2020) 71–76.
[8] Y. Chen, F. Sun, Z. Huang, et al., Appl. Catal. B: Environ. 215 (2017) 8–17.
[9] T. Xu, J. Wang, Y. Cong, et al., Chin. Chem. Lett. 31 (2020) 1022–1025.
[10] Z. Li, L. Zhang, Y. Liu, et al., Angew. Chem. Int. Ed. 59 (2020) 935–942.
[11] P. Zhang, S. Wang, B.Y. Guan, X.W. Lou, Energy Environ. Sci. 12 (2019) 164–168.
[12] D. Yuan, M. Sun, S. Tang, et al., Chin. Chem. Lett. 31 (2020) 547–550.
[13] W. Yang, X. Wang, S. Song, H. Zhang, Chem 5 (2019) 1743–1774.
[14] X. Yang, Y. Zhang, Y. Wang, et al., Chem. Eng. J. 387 (2020) 124100.
[15] K. Ye, Y. Li, H. Yang, et al., Appl. Catal. B: Environ. 259 (2019) 118085.
[16] M. Wang, M. Shen, X. Jin, et al., ACS Catal. 9 (2019) 4573–4581.
[17] W. Lei, T. Zhang, L. Gu, et al., ACS Catal. 5 (2015) 4385–4393.
[18] S. Bai, N. Zhang, C. Gao, Y. Xiong, Nano Energy 53 (2018) 296–336.
[19] M. Xiao, Z. Wang, M. Lyu, et al., Adv. Mater. 31 (2019) 1801369.
[20] H. Tong, S. Ouyang, Y. Bi, et al., Adv. Mater. 24 (2012) 229–251.
[21] Y.C. Zhang, M. Lei, K. Huang, et al., Mater. Lett. 116 (2014) 46–49.
[22] C. Zhang, X. Zhang, Y. Wang, et al., New J. Chem. 38 (2014) 2581–2586.

[23] X. Wang, Z. Li, J. Shi, Y. Yu, Chem. Rev. 114 (2014) 9346–9384.
[24] K. Zhou, Z. Yang, S. Yang, Chem. Mater. 19 (2007) 1215–1217.
[25] C. Pan, D. Zhang, L. Shi, J. Fang, Eur. J. Inorg. Chem. 2008 (2008) 2429–2436.
[26] X. Lu, D. Zheng, J. Gan, et al., J. Mater. Chem. 20 (2010) 7118.
[27] H.L. Tuller, Solid State Ion. 131 (2000) 143–157.
[28] M.V. Ganduglia-Pirovano, A. Hofmann, J. Sauer, Surf. Sci. Rep. 62 (2007) 219–270.
[29] J. Paier, C. Penschke, J. Sauer, Chem. Rev. 113 (2013) 3949–3985.
[30] G. Ou, Y. Xu, B. Wen, et al., Nat. Commun. 9 (2018) 1302.
[31] A.D. Liyanage, S.D. Perera, K. Tan, Y. Chabal, K.J. Balkus, ACS Catal. 4 (2014) 577–584.
[32] H. Zhang, C. Li, L. Lyu, C. Hu, Appl. Catal. B: Environ. 270 (2020) 118874.
[33] S. Zhan, H. Zhang, X. Mi, et al., Environ. Sci. Technol. 54 (2020) 8333–8343.
[34] Y. Huang, Y. Yu, Y. Yu, B. Zhang, Sol. RRL 4 (2020) 2000037.
[35] M. Kong, Y. Li, X. Chen, et al., J. Am. Chem. Soc. 133 (2011) 16414–16417.
[36] Y. Wang, J. Cai, M. Wu, et al., Appl. Catal. B: Environ. 239 (2018) 398–407.
[37] H. Tan, Z. Zhao, M. Niu, et al., Nanoscale 6 (2014) 10216–10223.
[38] Z. Li, K. Werner, K. Qian, et al., Angew. Chem. Int. Ed. 58 (2019) 14686–14693.
[39] Z. Su, W. Yang, C. Wang, et al., Environ. Sci. Technol. 54 (2020) 12684–12692.
[40] P. Trogadas, J. Parrondo, V. Ramani, ACS Appl. Mater. Interfaces 4 (2012) 5098–5102.
[41] W.H. Weber, K.C. Hass, J.R. McBride, Phys. Rev. B: Condens. Matter Mater. Phys. 48 (1993) 178–185.
[42] L.R. Shah, B. Ali, H. Zhu, et al., J. Phys. Condens. Matter 21 (2009) 486004.
[43] M.S.P. Francisco, V.R. Mastelaro, P.A.P. Nascente, A.O. Florentino, J. Phys. Chem. B 105 (2001) 10515–10522.
[44] H. Miao, G.F. Huang, J.H. Liu, et al., Appl. Surf. Sci. 370 (2016) 427–432.
[45] Y. Li, Q. Sun, M. Kong, et al., J. Phys. Chem. C 115 (2011) 14050–14057.
[46] P. Patsalas, S. Logothetidis, L. Sygellou, S. Kennou, Phys. Rev. B 68 (2003) 035104.
[47] L.T. Thanh, T.D.A. Quang, T.T.T. Toan, et al., J. Environ. Chem. Eng. 6 (2018) 5999–6011.